HAL
open science

Imaging the structural organization of chemical elements in growth cones of developing hippocampal neurons

Asuncion Carmona, Si Chen, Florelle Domart, Daniel Choquet, Richard Ortega

To cite this version:

Asuncion Carmona, Si Chen, Florelle Domart, Daniel Choquet, Richard Ortega. Imaging the structural organization of chemical elements in growth cones of developing hippocampal neurons. Metallomics, 2022, 14 (1), pp.mfab073. 10.1093/mtomcs/mfab073 . hal-03526688

HAL Id: hal-03526688

https://hal.science/hal-03526688v1

Submitted on 14 Jan 2022

HAL is a multi-disciplinary open access archive for the deposit and dissemination of scientific research documents, whether they are published or not. The documents may come from teaching and research institutions in France or abroad, or from public or private research centers.

L'archive ouverte pluridisciplinaire **HAL**, est destinée au dépôt et à la diffusion de documents scientifiques de niveau recherche, publiés ou non, émanant des établissements d'enseignement et de recherche français ou étrangers, des laboratoires publics ou privés.

Imaging the structural organization of chemical elements in growth cones of developing hippocampal neurons

Asuncion Carmona[1*], Si Chen[2], Florelle Domart[1,3], Daniel Choquet[3,4] and Richard Ortega[1*]

[1] Univ. Bordeaux, CNRS, CENBG, UMR 5797, 33170 Gradignan, France

[2] X-ray Science Division, Advanced Photon Source, Argonne National Laboratory, Lemont, IL 60439, USA

[3] Univ. Bordeaux, CNRS, Interdisciplinary Institute for Neuroscience, IINS, UMR 5297, 33000 Bordeaux, France.

[4] Univ. Bordeaux, CNRS, INSERM, Bordeaux Imaging Center, BIC, 33000 Bordeaux, France.

[*]Corresponding authors: acarmona@cenbg.in2p3.fr; ortega@cenbg.in2p3.fr

Mailing address: CENBG-CNRS, 19 chemin du solarium, 33175 Gradignan, France

Short running head: Chemical elements imaging in neuronal growth cones

Abstract

During neurodevelopment, neurons form growth cones, F-actin rich extensions located at the distal end of the neurites. Growth cones allow dendrites and axons to build synaptic connections through a process of neurite guidance whose mechanisms have not been fully elucidated. Calcium is an important element in this process by inducing F-actin reorganization. We hypothesized that other biologically active elements might be involved in the growth cone-mediated neurite guidance mechanisms. We performed super resolution and confocal microscopy of F-actin, followed by synchrotron X-ray fluorescence microscopy of phosphorous, sulfur, chlorine, potassium, calcium, iron and zinc on growth cones from primary rat hippocampal neurons. We identified two main patterns of element organization. First, active growth cones presenting an asymmetric distribution of Ca co-localized with the cytoskeleton protein F-actin. In active growth cones, we found that the distributions of P, S, Cl, K and Zn are correlated with Ca. This correlation is lost in the second pattern, quiescent growth cones, exhibiting a spread elemental distribution. These results suggest that Ca is not the only element required in the F-actin rich active regions of growth cones. In addition, highly concentrated Fe spots of sub-micrometer size were observed in calcium-rich areas of active growth cones. These results reveal the need for biological active elements in growth cones during neural development and may help explain why early life deficiencies of elements, such as Fe or Zn, induce learning and memory deficits in children.

KEYWORDS: hippocampal neurons, growth cones, metals, actin, STED, synchrotron imaging.

Introduction

A growth cone is a transient and mobile neuronal structure whose function is to explore the extracellular environment responding to neurite guidance molecules in order to reach a target organ during neurodevelopment. Growth cones are located at the distal end of growing axonal or dendritic extensions. The dynamic organization of two cytoskeleton proteins, actin and tubulin, governs the development of growth cones, resulting in filamentous (F)-actin and microtubules (MTs) polymers that promote shape changes and movement.[1] Therefore, the study of the molecular mechanisms governing the dynamic organization of the cytoskeleton structure in growth cones has drawn considerable attention in the recent years since these mechanisms are important in the understanding of neurodevelopment,[1] and in the investigation of axon-regeneration strategies on adult neurons.[2]

Calcium plays a central role in the regulation of cytoskeleton proteins during growth cones neurite pathfinding.[3,4] Calcium governs the organization of the cytoskeleton by regulating phosphorylation signaling cascades. Growth cones migrate following guidance cue gradients, shaping the growth cones with a higher receptor occupancy in the direction of the attractive guidance cue gradient. This asymmetric receptor distribution will result in the asymmetric distribution of the second messengers such as Ca in the direction of the attractive guidance cues. This asymmetric distribution of Ca in growth cones has been evidenced thanks to calcium-specific fluorescent markers.[5,6] However, the potential involvement of other elements during growth cone neurite pathfinding has not yet been investigated, probably due to the lack of appropriate element imaging methods.

Using synchrotron X-ray Fluorescence Microscopy (XFM), a high sensitivity multi-elemental imaging technique, we have previously shown that biological metals such as Cu and Zn are involved in the structural organization of F-actin and microtubules in dendrites and spines of mature hippocampal neurons.[7,8] Now we ask if a similar process could exist in growth cones from developing neurons and if other elements than Ca could play a role in the structural organization of the cytoskeleton.

In this purpose, we carried out synchrotron XFM to depict the distribution of P, S, Cl, K, Ca, Fe, and Zn in growth cones from developing primary rat hippocampal neurons. We applied our recently developed correlative imaging workflow combining synchrotron XFM and super resolution microscopy of F-actin and tubulin using STED (stimulated emission depletion) microscopy.[8] This high resolution and high sensitivity correlative imaging approach revealed the asymmetric distribution of most of the elements in growth cones suggesting their requirement in axonal and dendritic guidance.

Methods

Culture of primary rat hippocampal neurons

Hippocampal neurons from 18 days old embryonic rats (E18, Sprague−Dawley) were dissociated and cultured on an astrocyte feeder layer, as adapted from the protocol described by Kaech and Banker.[9] Neurons were grown at 37°C, 5% CO_2, in neurobasal medium (Gibco) supplemented with 2 mM L-glutamine and NeuroCult SM1 neuronal supplement (StemCell Technologies). The experimental designs and all procedures were in accordance with the European guide for the care and use of laboratory animals and the animal care guidelines issued by the animal experimental committee of Bordeaux University. In our protocol, silicon nitride membranes of 500 nm thickness (Silson Ltd.), which are compatible with synchrotron XFM, were used as culture substrate instead of glass coverslips.[8,10] Sterile silicon nitride membranes were coated beforehand with 1 $mg \cdot mL^{-1}$ poly-L-lysine in 0.1 M borate buffer (both from Sigma-Aldrich, France), for 2h at 37°C, washed twice with ultra pure sterile water and covered with neurobasal medium until used. 10,000 neurons in 10 µL neurobasal medium was uploaded over the membranes and neurons were allowed to adhere for 15 minutes in the incubator (37°C, 5% CO_2). Then neurobasal medium was gently added and neurons were cultured for 2 hours in the incubator before being transferred to a plate containing the astrocyte feeder layer, where they were left in culture until DIV3 (3 days *in vitro*).

Live-cell fluorescent labeling

Primary rat hippocampal neurons at DIV3 were labeled for live-cell microscopy of F-actin and tubulin using fluorogenic probes based on silicone rhodamine (SiR) from Spirochrome.[11,12] These fluorescent dyes can be imaged together using SiR and SiR700 fluorophores. SiR- and SiR-700-actin are based on the actin binding peptide jasplakinolid while SiR- and SiR-700-tubulin are based on the tubulin binding drug docetaxel. Following the instructions provided by the manufacturer, neurons were exposed to either 1 µM SiR-actin plus 1 µM SiR700-tubulin or 1 µM SiR-tubulin and 1 µM SiR700-actin. The fluorescent probes were added directly to the culture medium and the samples were incubated at 37°C and 5% CO_2 for 1.5h. The labeling was performed just prior to live-cell microscopy.

STED and confocal microscopy

STED and confocal microscopy were performed on a commercial Leica DMI6000 TCS SP8 X microscope. DIV3 neurons cultured on silicon nitride membranes and labeled with SiR fluorogenic probes were maintained in the microscope chamber at 37°C in a pre-warmed Tyrode's solution (NaCl 135 mM, KCl 5 mM, $CaCl_2$ 1.8 mM, $MgCl_2$ 0.4 mM, glucose 1 mM, HEPES 1 mM, pH 7.4 and 240 mOsm). The osmolarity of Tyrode's solution was measured with a vapor pressure osmometer (VAPRO® 5600, Elite) and adjusted to the initial values of the Neurobasal culture medium (240 mOsm). For live cell microscopy, the silicon nitride membranes were mounted in a Ludin chamber, with neurons facing the coverslip to minimize the distance between the objective and neurons.

Confocal and STED images were acquired with a HC-PL-APO-CS2 93x glycerol immersion objective with a numerical aperture of 1.3 and a scan speed of 200 Hz. For excitation of SiR fluorogenic probes, a supercontinuum laser from 470 nm to 670 nm was set to 640 nm (SiR channel) or 670 nm (SiR700 channel). The emission was recorded with a Leica HyD detector (hybrid detector) with a spectral range from 651 to 680 nm for SiR channel and from 710 to 760 for SiR700 channel. For STED

acquisitions we used a 775 nm pulsed diode laser. The images were acquired using the Leica Application Suite X software (LAS X). The physical length of STED images was set to 25 µm side and the pixel size was fixed at 24 nm. Largest confocal images were made with a length of 125 µm and a pixel size of 61 nm. The x,y positions of each growth cones were recorded in order to calculate the relative positions respectively to the membrane's corners, and to find these positions on the synchrotron setup.[8]

Sample preparation for XFM

For synchrotron XFM analysis, samples were cryo-processed by plunge-freezing and freeze-dried. This method of cryo-processing enables to preserve the structure and the chemical element composition of neurons.[7,8,10] After live-cell microscopy, samples were rinsed with an ammonium acetate buffer solution adjusted to pH 7.4 and 240 mOsm in ultra trace elemental analysis grade water (Fisher Scientific). This rinsing allows to remove, from the surface of the samples, the remaining salts of the Tyrode's solution. After washing, ammonium acetate was blotted with ashless, ultra-absorbent paper (Whatman), by capillarity from the sides of the membrane avoiding contact with neurons. Then the samples were quickly plunged in liquid methylbutane cooled with liquid nitrogen (-164°C), for about 15 seconds. After plunge-freezing, the excess methylbutane remaining on the silicon nitride membranes was absorbed with an ashless ultra-absorbent filter paper, keeping the samples at all time in liquid nitrogen vapors.

After plunge-freezing, the samples were freeze-dried using a Christ alpha 2-4 LD plus freeze-dryer. Once the device was working at -75°C for at least one hour, the samples were introduced quickly (keeping the temperature of the samples below -50°C) and the freeze-drying procedure was launched for 48 hours under a primary vacuum ($2 \cdot 10^{-3}$ mbar). After this time, the freeze-dryer was turned off, allowing the temperature to gradually rise up to room temperature. At this point, dry air was slowly blown into the device and the samples were kept in a desiccator at room temperature until use.

Because freeze-drying can slightly alter the morphology of the cells, we systematically verified the neuronal preservation of the regions that will be further analyzed by synchrotron XFM after cryo-processing. Confocal microscopy of actin and tubulin was performed on freeze-dried samples on the regions of interest selected during live-cell microscopy to check for adequate sample preservation.[8]

Synchrotron XFM and data analysis

Synchrotron XFM measurements were performed at the Bionanoprobe[13] at the Advanced Photon Source (APS) of Argonne National Laboratory. 10 keV monochromic X-ray photons were focused on the samples with Fresnel zone plates. The pixel size varied between 85-200 nm depending on the scan size and analysis time, and maintaining a flux of 10^9 photons/s and a maximum integration time of 2s per pixel. While a sample was raster scanned across the incident X-ray beam, a full X-ray fluorescence spectrum at each pixel was acquired using a 4-element silicon drifted detector (Vortex ME4, Hitachi High-Technologies Science America). The spectra were then fitted and quantified by comparing to a standard thin film (RF8-200-S2453, AXO Dresden GmbH) measured in the same condition using MAPS software.[14] Elements such as P, S, Cl, Ca, K, Fe and Zn could be detected and imaged in growth cones but not copper which was below the detection limit. 2D XFM elemental distributions presented in this article are shown in Fig. S4.

Image analysis and statistics

For Pearson's and Mander's coefficients calculation[15] the procedure was as follows. Using Image J software,[16] in each original XFM image, the mean intensity value and standard deviation (SD) were measured in blank areas, outside the growth cones, to define the background signal. Then the images were thresholded setting to zero all the pixels with intensity values below the mean plus 3 times the SD of the blank areas. On the thresholded images, Pearson's and Mander's coefficients were calculated using EzColocalization plugin.[17] The Pearson's coefficient is a measure of the linear correlation between the distributions of two given elements, based on their respective XRF signal intensity per pixel. The Mander's coefficients inform about the overlap existing for the different pixels that make up the image between one element and another. M1 indicates how many pixels (above the background) of the upper elements in the first line of the table co-occurs with the pixels of the right-hand elements. M2 indicates the overlapping in the opposite way, how many pixels of the right-hand elements overlaps with pixels of the top elements.

For plotting elemental profiles all together, GraphPad Prism 8 software was used (http://www.graphpad.com/). In this case, the intensity of x-ray counts was normalized to adjust the maximum values to 1 for each element.

Results

Element distribution in growth cones.

Using synchrotron XFM we revealed the distribution of P, S, Cl, K, Ca, Fe and Zn in growth cones from primary hippocampal neurons cultured *in vitro* during 3 days (DIV3) after dissociation from rat E18 embryos. Fig. 1, 2, 3, 6 and S2 are representative of the main feature of elemental distribution observed, with an asymmetric Ca layout within a narrow region of the growth cone. In the second feature, we observed a spread out distribution of Ca all over the growth cone (Fig. 4 and S3).

In the first category of elemental distribution (Fig. 1, 2, 3, 6 and S2), Ca is present in an asymmetric narrow region of the growth cone, together with other elements (P, S, Cl, and Zn). This type of elemental distribution happened either in palm-shape growth cones (Fig. 1, 6 and S2), or in bundled growth cones (Fig. 2, 3).

In the second category of elemental distribution (Fig. 4 and S3), Ca as well as P, S, Cl, and Zn are distributed in a widespread area of the growth cones. The intensity of Ca signal is relatively lower in growth cones with a Ca widespread distribution compared to the ones with asymmetric Ca content, as illustrated in Fig. S1 showing on the same image a group of growth cones using a large XFM scan (20 µm x 20 µm).

In all cases (Fig. 1, 2, 3, 4, 6, S2 and S3), K distribution is heterogeneous and it is the only element present in the whole area of the growth cones, as illustrated by the white line of K boundary in Fig. 1.

In all growth cones, Fe is observed in a limited number of small dotted structures (Fig. 1, 2, 3, 4, 6, S1, S2 and S3). Iron-rich dots sizing from single pixels (85 nm) to a few hundred nanometers have been systematically observed in all the analyzed samples. Although Fe has a dotted distribution, distinct from that of the other elements, in growth cones showing an asymmetric Ca distribution, Fe is located within the Ca-rich area, at the distal end of this area (Fig. 1, 2, 3, S1and S2). In growth cones

showing a wide spread distribution of calcium (not asymmetric), Fe is not detected in the growth cones (Fig. S1) but is present as hot spots in the neurite shaft (Fig. 4, S1 and S3).

Finally, P, S, Cl, K, Ca and Zn are homogeneously distributed all along the neurite shafts (Fig. 1, 2, 3, 4, S1, S2 and S3). This is particularly well illustrated in Fig. 2 by the element distribution along the thin neurite bordering the growth cone.

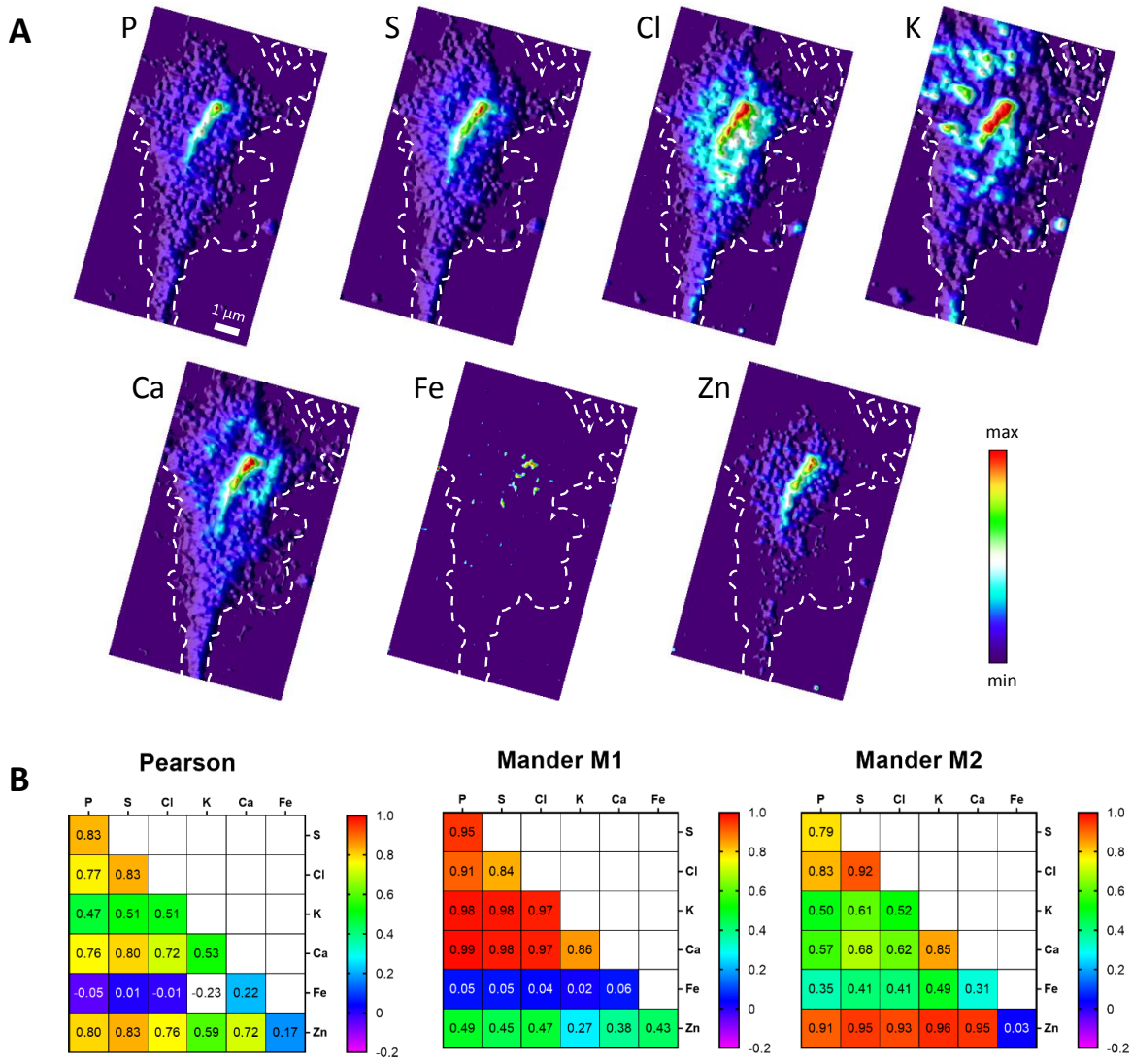

Fig. 1 (A) Synchrotron XFM multi-elemental imaging showing the asymmetric distribution of Ca in a palm-shaped growth cone from a primary rat hippocampal neuron. K contours are outlined (dotted line) to highlight the singular distribution of this element, the only one being present into the whole growth cone area. Scan size: 7 µm x 12 µm and pixel size: 150 nm. X-ray counts displayed with a color scale from minimum (blue) to maximum (red). (B) Pearson's correlation and Mander's overlap coefficients between elements.

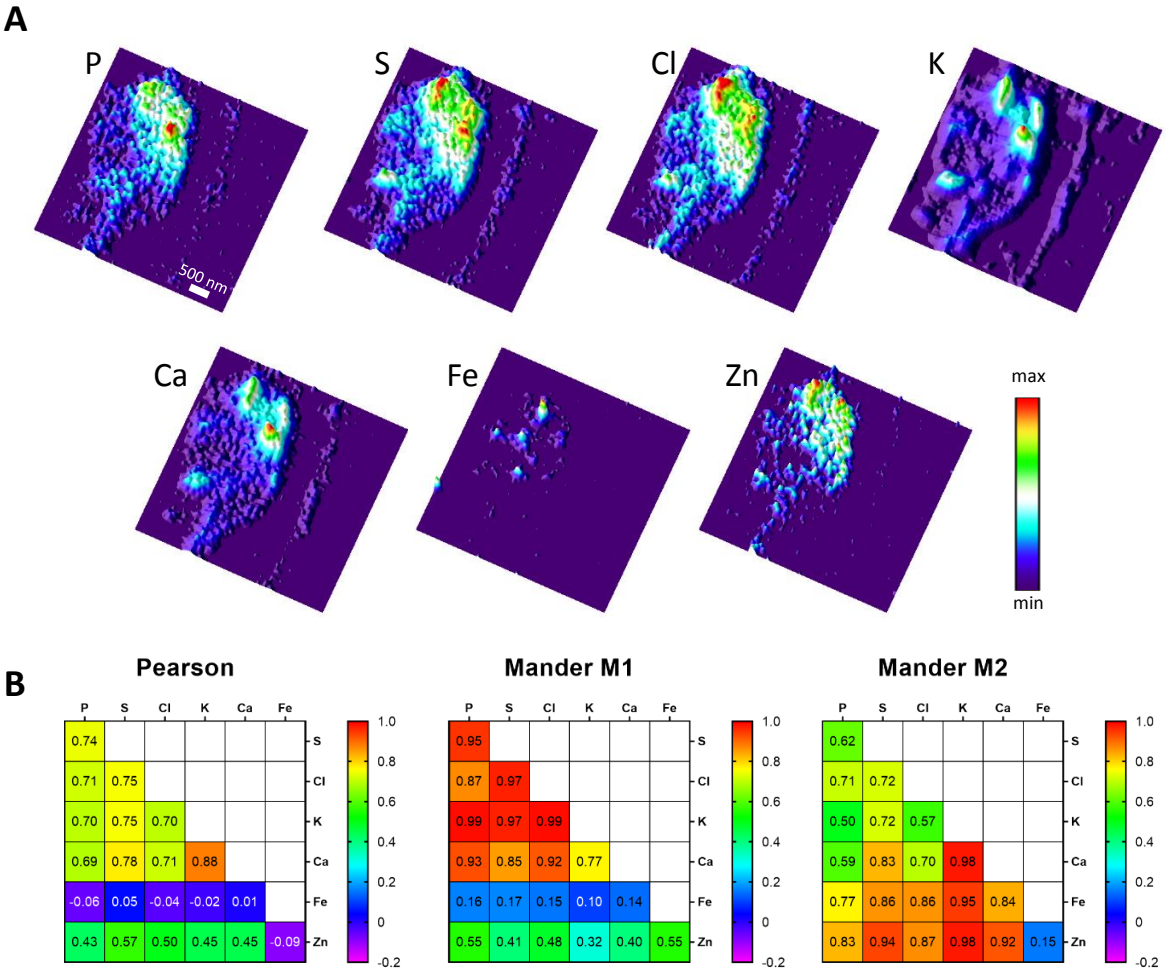

Fig. 2 (A) Synchrotron XFM multi-elemental imaging showing the asymmetric distribution of Ca in a bundled growth cone from a developing primary rat hippocampal neuron. A thin neurite outgrowth is visible on the right of the image, parallel to the growth cone. Scan size: 5 µm x 5 µm and pixel size: 85 nm. X-ray counts displayed with a color scale from minimum (blue) to maximum (red). (B) Pearson's correlation and Mander's overlap coefficients between elements.

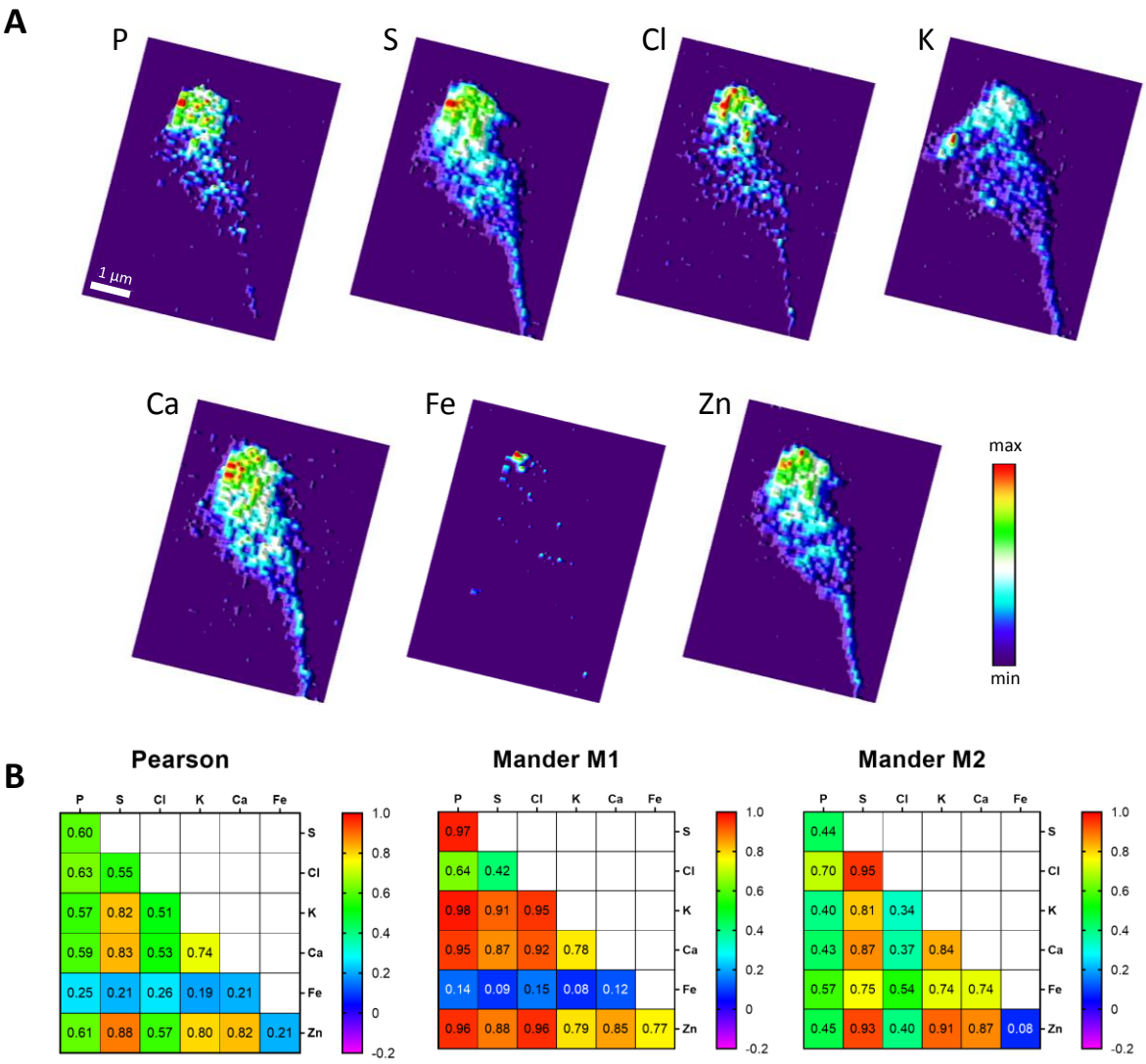

Fig. 3 (A) Synchrotron XFM multi-elemental imaging showing the asymmetric distribution of Ca in a bundled growth cone from a primary rat hippocampal neuron. Scan size: 9 µm x 6.5 µm and pixel size: 150 nm. X-ray counts displayed with a color scale from minimum (blue) to maximum (red). (B) Pearson's correlation and Mander's overlap coefficients between elements.

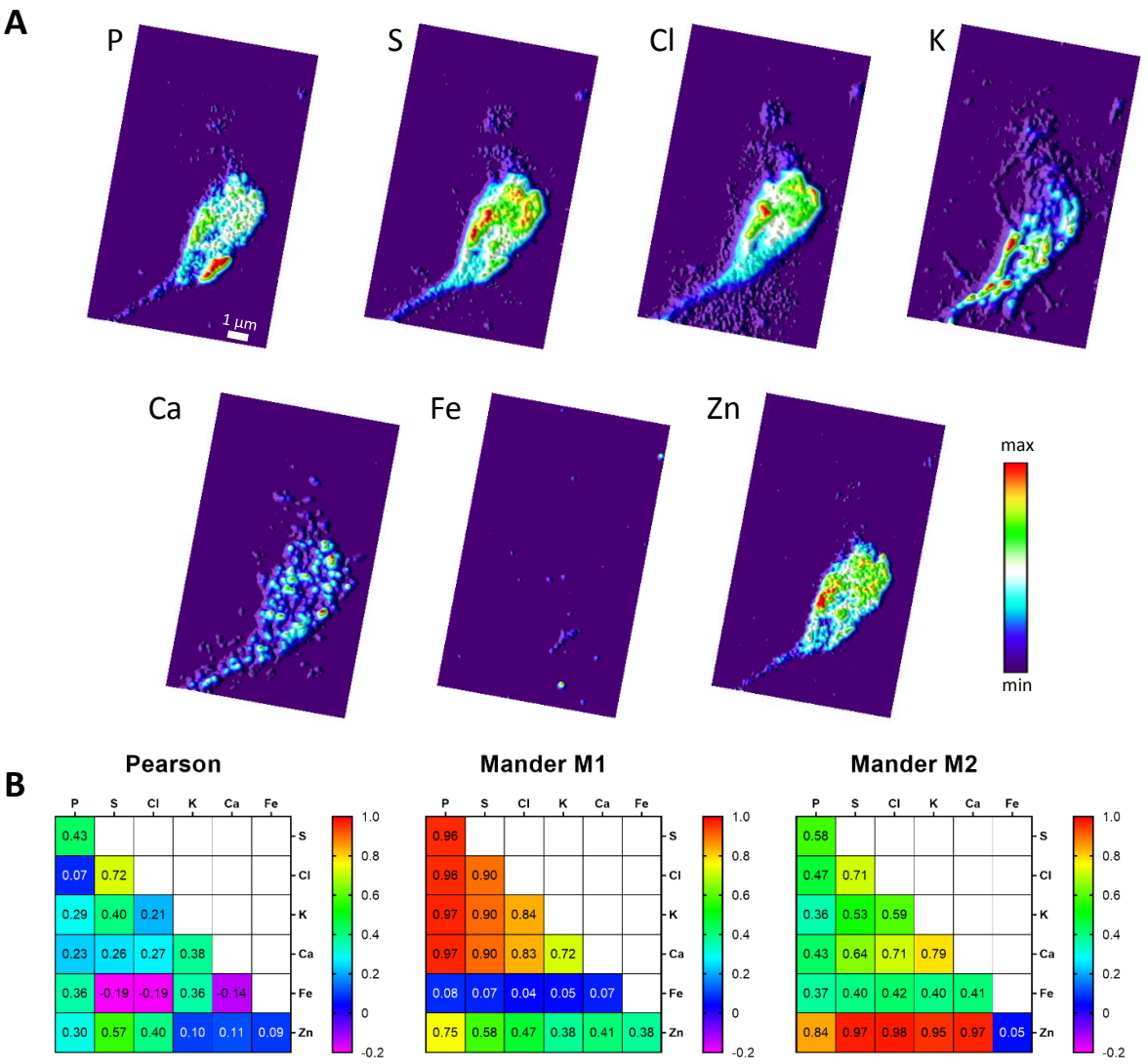

Fig. 4 (A) Representative example of synchrotron XFM multi-elemental imaging showing the widespread distribution of Ca in a growth cone from a primary rat hippocampal neuron. Scan size: 8.6 µm x 14.3 µm and pixel size: 150 nm. X-ray counts displayed with a color scale from minimum (blue) to maximum (red). (B) Pearson's correlation and Mander's overlap coefficients between elements.

Element co-localization in growth cones.

In all cases, the distribution of Fe is not correlated with any of the other elements, showing the lowest Pearson's and Mander's coefficients (Fig. 1, 2, 3 and 4), meaning that Fe has a completely different distribution from the other elements.

In growth cones with asymmetric Ca distribution (Fig. 1, 2 and 3), moderate to strong positive correlations between elements are measured for P, S, Cl, K, Ca, and Zn showing moderate to high Pearson's correlation coefficients. Except for Fe, M1 and M2 coefficients show a large overlap index, between all the chemical elements, either in one direction or in the other. Mander's coefficient indicate that a co-localization exists between elements, but some exhibit a more expanded distribution than others do. For example, P and K distributions show a very high M1 coefficient (from

0.98 to 0.99) but moderate M2 coefficient (from 0.40 to 0.50), meaning that both can be found in the same pixels, but that in some areas of the growth cone there is K but no P.

In a growth cone with a Ca widespread distribution (Fig. 4), the strong correlation between elements is lost, as illustrated by the low Pearson's correlation coefficients values.

Correlative imaging of elements and cytoskeleton proteins in growth cones

Using live-cell confocal microscopy we imaged large areas showing whole neurons at DIV3 labeled with silicon rhodamine (SiR)-actin and SiR-tubulin fluorescent dyes to locate growth cones (Fig. 5A), and then we performed live-cell STED microscopy to image smaller areas of 25 µm x 25 µm centered in growth cones (Fig. 5B-D). As expected from the known distribution of cytoskeleton proteins in growth cones,[1-2,18-19] we observed a strong compartmentalization of tubulin and F-actin, with tubulin in the central domain and F-actin in the peripheral domain. As schematized in Fig. 5E, the central domain is structured by microtubules arising from the dendritic shaft and the peripheral domain is rich in F-actin, forming lamellipodia and filopodia from actin filaments and actin patches.

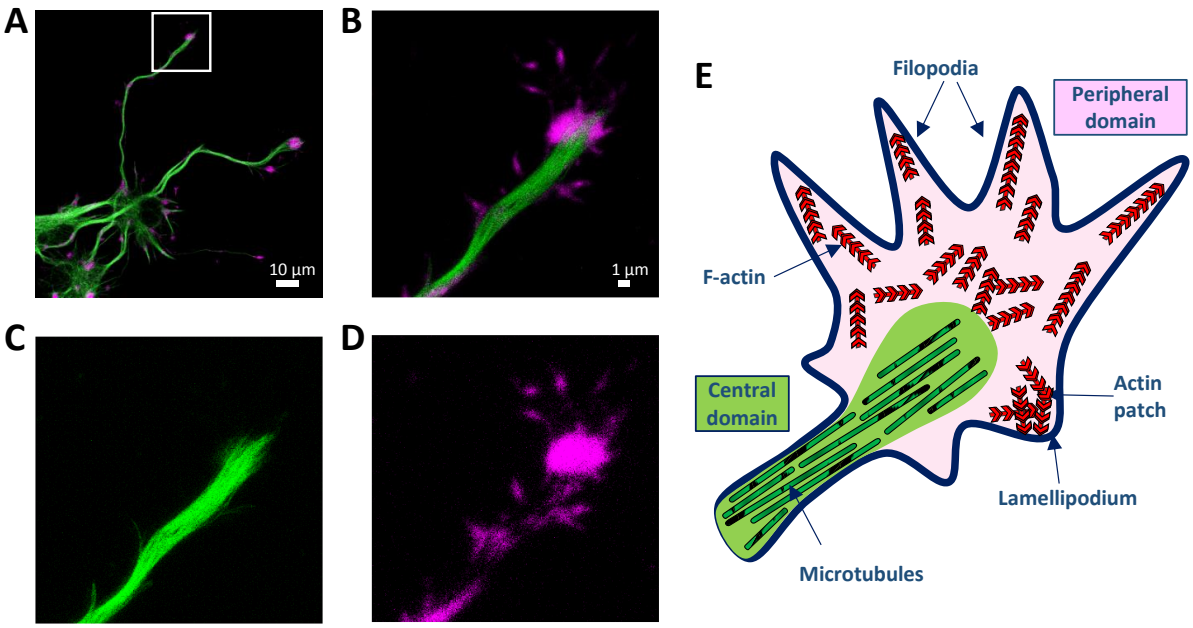

Fig. 5 Confocal and STED microscopy of F-actin (magenta) and tubulin (green) in growth cones labeled with SiR700-actin and SiR-tubulin fluorescent dyes. (A) Merged confocal microscopy image of F-actin and tubulin showing several growth cones at the distal ends. (B) Merged confocal image of F-actin and STED microscopy of tubulin in the single growth cone framed in A (white square). (C) STED microscopy image of tubulin alone. (D) Confocal microscopy image of F-actin alone. (E) Schematic representation of a growth cone showing the two main domains, central (in green) and peripheral (in pink).

Spatial alterations in growth cone Ca concentration can direct neurite growth and protrusion by modulating the expression of cytoskeleton proteins.[4] In order to better interpret our results on Ca

but also on other elemental distributions, we performed a correlative microscopy approach that enables the imaging of chemical elements and cytoskeleton proteins at high spatial resolution (Fig. 6, 7, 8).[8] STED microscopy of SiR-actin and SiR-tubulin was carried out before cryo-processing, on living cells (Fig. 6A), and after cryo-processing, on freeze-dried cells (Fig. 6B), and compared with synchrotron XFM imaging of element distributions (Fig. 6C). Potassium distribution shows that the palm-shaped morphology of the growth cone is maintained after cryo-processing although a shrinkage of the F-actin distribution is observed when comparing images before and after cryo-processing (Fig. 6A and B). Most of the elements are concentrated in the F-actin rich-region, being K the element displaying the most spread out distribution.

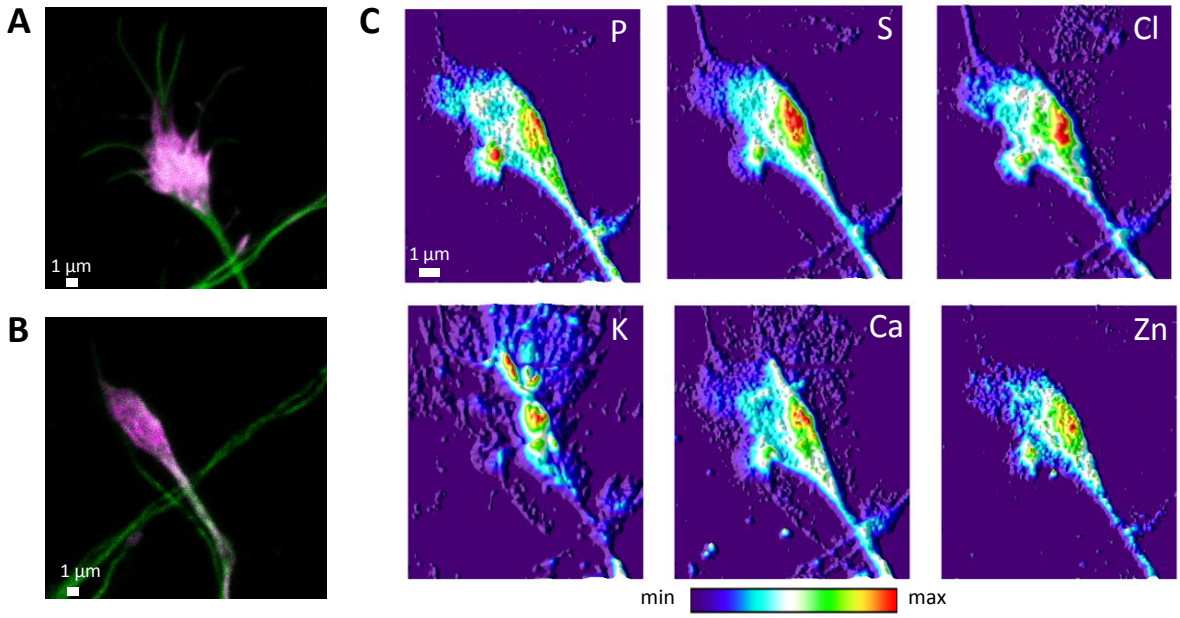

Fig. 6 Combined high-resolution imaging of cytoskeleton proteins and chemical elements in a growth cone. (A) Live-cell merged image of tubulin confocal microscopy (green) and F-actin STED microscopy (magenta) labelled respectively with SiR700-tubulin and SiR-actin fluorescent probes. (B) Tubulin (green) and F-actin (magenta) confocal microscopy merged image, on the same growth cone, after sample plunge-freezing and freeze drying. (C) Synchrotron XFM multi-elemental imaging. Scan size 11.5 µm x 13.5 µm and pixel size 85 nm.

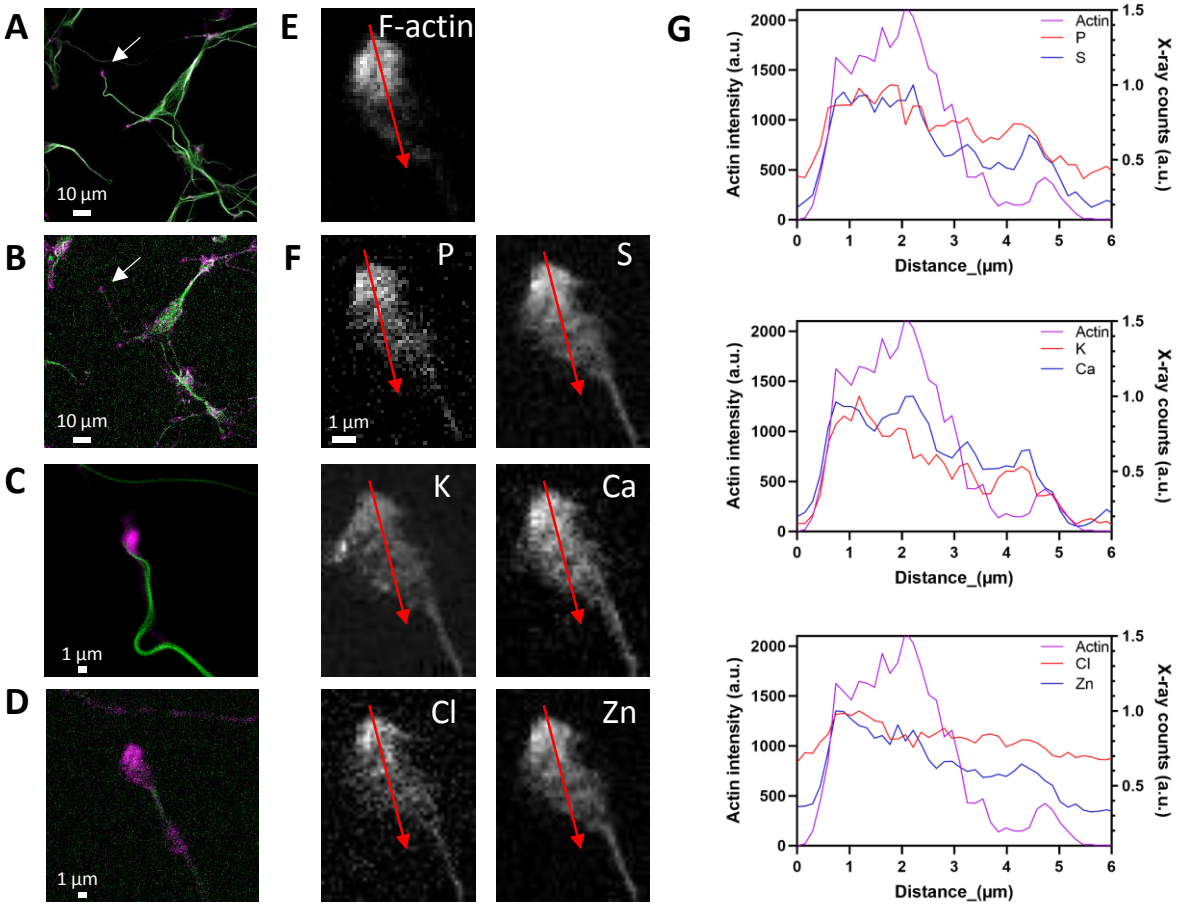

Fig. 7 Correlative imaging of cytoskeleton proteins and chemical elements in a growth cone showing an asymmetric Ca distribution. (A) Tubulin (green) and F-actin (magenta) live-cell confocal imaging on a primary rat hippocampal neuron at DIV3. (B) Confocal microscopy on the same neuron after plunge-freezing and freeze-drying. (C) Live-cell merged image of tubulin STED microscopy and F-actin confocal microscopy (labelled respectively with SiR and SiR700 probes) on the growth cone pointed out in A (arrow). (D) Confocal images at the tip of the growth cone after plunge-freezing and freeze-drying. (E) Distribution of F-actin after freeze-drying trimmed to the same size as the XFM analysis. (F) Synchrotron XFM element distributions in the growth cone. Scan size: 9 µm x 6.5 µm and pixel size: 150 nm. (G) Plot profiles of F-actin and element distributions across the red line drawn in E) and F). Fluorescence intensity of F-actin and X-ray counts normalized intensity for each element are presented with arbitrary units (a.u.).

From Fig. 7, in growth cones showing an asymmetric Ca distribution, it can be deduced that P, S, Cl, Ca and Zn follow the same concentration gradient as the one of F-actin. From plot profiles, we evidence an increase on element distribution in the region where F-actin fluorescence intensity is higher. From Fig. 8, in growth cones showing a widespread Ca distribution, the elements do not follow the F-actin gradient distribution.

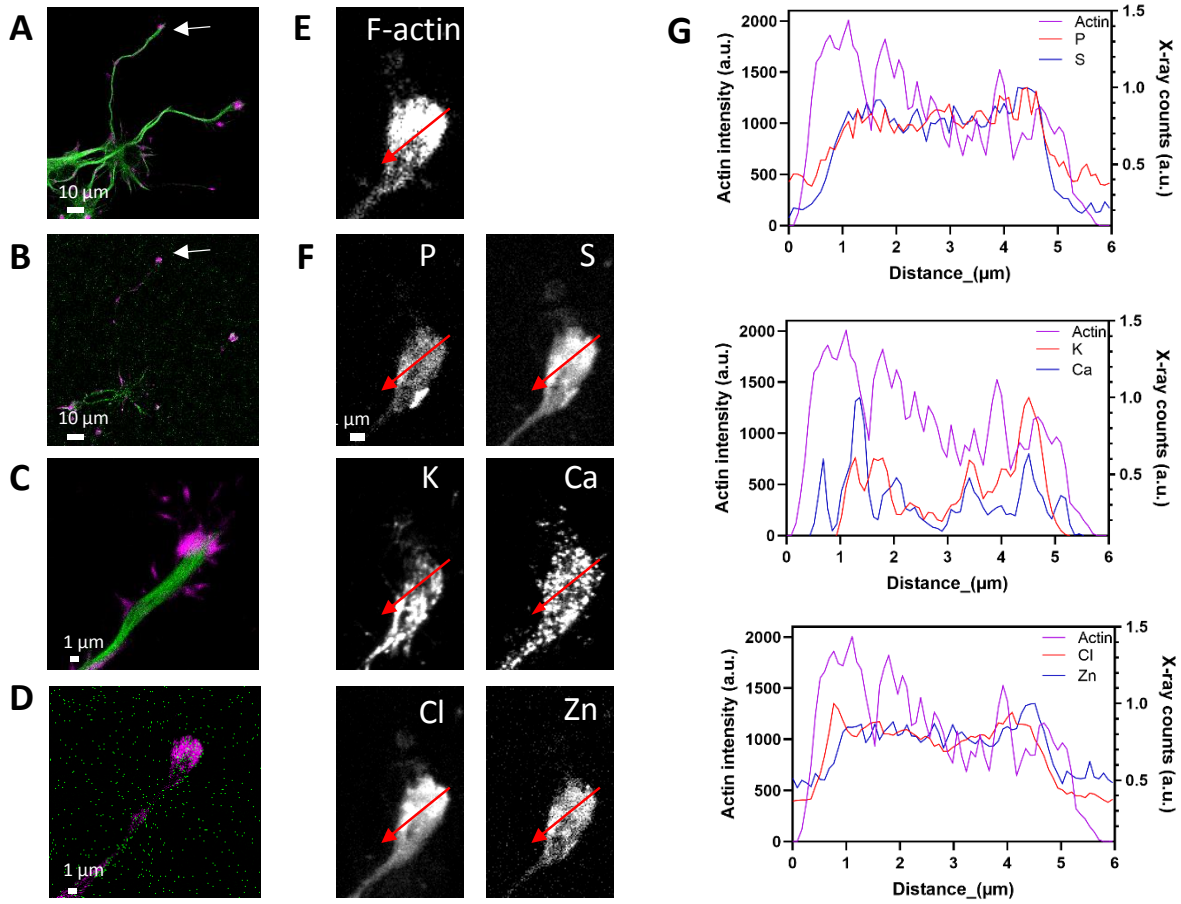

Fig. 8 Correlative imaging of cytoskeleton proteins and chemical elements in a growth cone showing a widespread Ca distribution. (A) Live-cell confocal imaging of tubulin (green) and F-actin (magenta) on a primary rat hippocampal neuron at DIV3. (B) Confocal microscopy on the same neuron after plunge-freezing and freeze-drying. (C) Live-cell merged image of tubulin STED microscopy and F-actin confocal microscopy (labelled respectively with SiR and SiR700 probes) on the growth cone pointed out in A (arrow). (D) Confocal images of tubulin (green) and F-actin (magenta) of the growth cone after plunge-freezing and freeze-drying. (E) Distribution of F-actin after freeze-drying trimmed to the same size as the XFM analysis. (F) Synchrotron XFM elements distribution in the growth cone. Scan size: 8.6 µm x 14.3 µm and pixel size: 150 nm. (G) Plot profiles of F-actin and elements distribution across the red line drawn in E) and F). Fluorescence intensity of F-actin and X-ray counts normalized intensity for each element are presented with arbitrary units (a.u.).

Discussion

As expected from the known cytoskeleton organization of growth cones in developing neurons, we found that growth cones from DIV3 primary rat hippocampal neurons exhibit a strong compartmentalization of tubulin and F-actin, with tubulin in the central domain and F-actin in the peripheral domain (Fig. 5).[1-2,18-19] In the peripheral domain, F-actin forms patches in lamellipodia promoting axon outgrowth, and bundles in filopodia that sense guidance cues.

Calcium distribution in growth cones

Spatial alterations in growth cone Ca concentration can direct neurite growth.[4,20] Global increases in the spatial distribution and amplitude of Ca control stopping, pausing and collapse,[3,21-22] whereas small, spatially localized elevations of Ca can effectively steer growth cones *in vitro*.[5,6] Calcium controls the growth cone cytoskeleton by regulating phosphorylation signaling cascades.[4]

Fluorescence microscopy using Ca^{2+} specific fluorescent dyes has provided a wealth of information about Ca localization in growth cones during axonal guidance in neurodevelopment. For example, fluo-3 imaging, a fluorescent indicator of intracellular Ca, has shown the focal increase of Ca^{2+} in *Xenopus* growth cones at the site of guidance cues induction.[5] Using the CaGD-1 Ca imaging dye on retinal ganglion cell growth cones, Ca is present mostly in the central region of quiescent growth cones while in growth cones with spontaneous activity Ca spiking was observed in the distal tip.[23] Tracing of Ca activity in growth cones can also be imaged by electroporating developing neurons with GCaMP2, a fluorescent genetically encoded Ca indicator. This technology was applied to study axonal outgrowths of callosal neurons showing that Ca is increased at the tip of the growth cone, whereas when axonal extension is inhibited it results in the accumulation of Ca in the central domain.[24] Similarly, using the membrane bound Ca indicator Fluo4 MOMO, it was found that Ca is present as dotted structures in the central region of the quiescent growth cones, then after activation Ca displays a more compact and asymmetric distribution at the tip of the growth cone.[25]

In agreement with these reports, our observations regarding Ca distributions can be classified into to two main patterns, an asymmetric arrangement of Ca with higher accumulation at the distal end corresponding to the growth cones in active phases of development (Fig. 1, 2, 3, 6, 7, S1 and S2), and a spread distribution of ca in the central domain corresponding to a quiescent state (Fig. 4, 8, S3).

The central domain of growth cones is rich with microtubules and organelles, such as the endoplasmic reticulum (ER). The dotted Ca distribution in the central domain of the growth cones is compatible with the presence of ER in this domain. Ca^{2+} release from the ER determines growth cone turning polarity.[3] Asymmetric Ca signals drive lamellipodial and filopodial protrusions.[3,4,20,26] Calcium signaling is followed by a cascade of events resulting in the asymmetric localization of cytoskeleton proteins such as β-actin,[27] and asymmetric cytoskeletal remodeling.[20] Our results are in good agreement with the expected distribution of Ca in quiescent neurons, and with Ca asymmetric redistribution during growth cone activation and co-localization with F-actin.

P, S, Cl, K and Zn distributions in growth cones

Except for Ca distribution, the localization of other chemical elements in growth cones was unknown. We found out that K is present in larger areas of the growth cone than any other element. This is in agreement with the known ubiquitous intracellular distribution of K ions that fill the whole intracellular volume. Potassium distribution obtained by XFM imaging can be used to display the cell boundaries.[28] In the present study, K distribution depicts the growth cone boundaries as well exemplified in Fig. 1. Potassium distribution is however not uniform and can show some asymmetry as it will be discussed below for the other elements.

We could highlight that P, S, Cl, K and Zn distributions were asymmetric in growth cones that present an asymmetric distribution of Ca (Fig. 1, 2, 3, 6, S2). It can be assumed that all these elements are needed at the active regions of the growth cone, rich in F-actin (Fig. 7). These results indicate that elements preferentially accumulate in the peripheral domain of the growth cone, that can be explained by a greater requirement for these elements in the F-actin rich areas, involved in cytoskeleton remodeling and formation of protrusions. Our results indicate that not only Ca is involved in the asymmetric modeling of the cytoskeleton, but that other elements are recruited to fulfil the metabolic activity generated by neurite guidance.

Iron distribution in growth cones

Iron-rich dots were observed within all the analyzed growth cones. Fe distribution did not correlate with any of the other chemical elements. However, in growth cones displaying asymmetric Ca distribution, Fe dots were located in the calcium-rich areas (Fig. 1, 2, 3, 6 and S2), at the distal end. This is the first direct evidence for the existence of iron-rich regions within growth cones. In a previous study we also found that similar Fe hot-spots accumulated in the distal end of differentiated PC12 cells.[28]

In growth cones showing a Ca widespread distribution, Fe-rich structures were located in the dendritic shaft and were less in number than in the Ca asymmetric growth cones (Fig. 4 and S3). This last observation is similar to our recent results of XFM element imaging in dendrites of mature (quiescent) hippocampal neurons, where Fe hot spots of 100-200 nm size were detected only in the dendrites contiguous to the dendritic spines but not in the spines.[8] Our results suggest that in growth cones with Ca widespread distribution, representing quiescent growth cones, iron-rich dots are present at low density in the dendritic shaft, similarly to what was observed for mature neurons.

The exact nature of these Fe-rich structures remains to be identified. Fe could be present within mitochondria where it is required for energy metabolism.[29] Iron-rich hot-spots have been tentatively identified as mitochondria using XFM.[30] Fe dotted structures could correspond to mitochondria both within the dendritic shafts of quiescent growth cones, and within the tips of the active growth cones. It has been reported that in inactive axons, mitochondria do not significantly enrich at the growth cone while in actively differentiating axons, mitochondria travel to the axonal growth cone.[31] Another hypothesis is that Fe could be present in ferritin-like structures. For axonal pathfinding, active growth cones require metabolic enzymes including ferritin. Ferritin mRNAs have been imaged by FISH (fluorescent *in situ* hybridization) on *Xenopus* growth cones.[32]

Expected consequences in case of element deficiency

Our results indicate that Fe-rich entities are expressed in active growth cones presumably to support the metabolic and/or energy requirements of the growth cone during neurite pathfinding. This observation has an important impact in our understanding of Fe functions during neurodevelopment and might help explain the deleterious effects of early-life iron-deficiency during the hippocampus development,[33] known to result in learning and memory deficits in children.[34] Iron deficiency is the most common nutrient deficiency affecting billions people worldwide, especially pregnant women and their offspring. Our data indicate an essential function for Fe in the neurite pathfinding process during neurodevelopment that could be irreversibly impaired in case of inadequate iron-availability.

Similarly, Zn deficiency is known to alter neurodevelopment.[35] Zinc deficiency is less frequent than iron-deficiency but is common worldwide, with an estimation of 17% of the global population at risk for inadequate Zn uptake and up to 30% in South Asia.[36] Our study also reveals the specific need of Zn in the active phases of growth cone development. This result is in line with studies on animal models of accelerated natural aging showing that Zn deficiency occurs in regions of the hippocampus.[37]

Conclusion

High resolution imaging using synchrotron XFM allowed us to describe the organization of chemical elements in the growth cones of primary rat hippocampal neurons. We have highlighted the existence of two characteristic distributions. On the one hand, an asymmetric distribution of Ca, P, S, Cl, K and Zn that could correspond to the active stages of neurite guidance. Iron also shows an asymmetric distribution, but in the form of submicrometer size aggregates. In contrast, in a smaller number of cases, the Ca distribution is widespread, not asymmetric, as for P, S, Cl and Zn while Fe is not detected in these growth cones. In all cases, the distribution of K is more extensive than that of the other elements and describes the entire surface of the growth cone. While the distribution of Ca in growth cones had been described previously, that of the other elements had not. Our study indicates the necessary mobilization of the main biologically relevant chemical elements inside the growth cones for neurite pathfinding, following the distribution of F-actin.

Neurite pathfinding is a critical process in the early stages of neurodevelopment to connect neurons to their partner structures to build the nervous system. We have shown that essential elements such as Ca, P, S, Cl, Fe and Zn are mobilized during this process, probably to fulfill energetic and metabolic functions of the growth cone. A lack of these elements in the critical period of neurodevelopment, especially Zn or Fe which may be deficient in the diet, would affect the growth cone neurite pathfinding and could lead to abnormal neurodevelopment. We have described in previous work the interplay between trace metals (e.g. Cu and Zn) and the architecture of the neuronal cytoskeletal in the formation of synaptic structures.[7,8] Here we have extended this concept to earlier stages of neuronal differentiation such as neurite pathfinding. Further work is planned to understand precisely the molecular mechanisms involving these elements in neurodevelopment phases.

Conflicts of interest

We declare no conflicts of interest.

Acknowledgements and Funding

We acknowledge Magali Mondin from Bordeaux Imaging Center, part of the France BioImaging national infrastructure, for her support in microscopy. We thank Emeline Verdier and Natacha Retailleau from IINS Cell Biology facility for hippocampal neurons supply. We are grateful to Olivier Thoumine (IINS) for providing useful discussions. This research received funding from Centre National de la Recherche Scientifique (CNRS), MITI Interdisciplinary Program, IDEX Bordeaux (PEPS CorXsyn), Interdisciplinary PhD program from the University of Bordeaux, ERC grant ADOS (339541) and DynSynMem (787340), and support from the Regional Council Nouvelle Aquitaine. This research used resources of the Advanced Photon Source, a U.S. Department of Energy (DOE) Office of Science User Facility, operated for the DOE Office of Science by Argonne National Laboratory under Contract No. DE-AC02-06CH11357. We are grateful to APS staff for assistance in using 9-ID-B Bionanoprobe beamline.

Data Availability

The data underlying this article will be shared on reasonable request to the corresponding author.

References

1. Dent EW, Gupton SL, Gertler FB. The growth cone cytoskeleton in axon outgrowth and guidance. Cold Spring Harb Perspect Biol. 2011, 3 (3), a001800. doi: 10.1101/cshperspect.a001800.

2. Blanquie O, Bradke F. Cytoskeleton dynamics in axon regeneration. Curr Opin Neurobiol. 2018, 51, 60-69. doi: 10.1016/j.conb.2018.02.024.

3. Tojima T, Hines JH, Henley JR, Kamiguchi H. Second messengers and membrane trafficking direct and organize growth cone steering. Nat Rev Neurosci. 2011, 12 (4), 191-203. doi: 10.1038/nrn2996

4. Gasperini RJ, Pavez M, Thompson AC, Mitchell CB, Hardy H, Young KM, Chilton JK, Foa L. How does calcium interact with the cytoskeleton to regulate growth cone motility during axon pathfinding? Mol Cell Neurosci. 2017, 84, 29-35. doi: 10.1016/j.mcn.2017.07.006.

5. Zheng JQ. Turning of nerve growth cones induced by localized increases in intracellular calcium ions. Nature. 2000, 403 (6765), 89-93. doi: 10.1038/47501.

6. Gomez TM, Robles E, Poo M, Spitzer NC. Filopodial calcium transients promote substrate-dependent growth cone turning. Science. 2001, 291 (5510), 1983-1987. doi: 10.1126/science.1056490.

7. Perrin L, Roudeau S, Carmona A, Domart F, Petersen JD, Bohic S, Yang Y, Cloetens P, Ortega R. Zinc and Copper Effects on Stability of Tubulin and Actin Networks in Dendrites and Spines of Hippocampal Neurons. ACS Chem Neurosci. 2017, 8 (7), 1490-1499. doi: 10.1021/acschemneuro.6b00452.

8. Domart F, Cloetens P, Roudeau S, Carmona A, Verdier E, Choquet D, Ortega R. Correlating STED and synchrotron XRF nano-imaging unveils cosegregation of metals and cytoskeleton proteins in dendrites. Elife. 2020, 9, e62334. doi: 10.7554/eLife.62334.

9. Kaech S, Banker G. Culturing hippocampal neurons. Nat Protoc. 2006, 1 (5), 2406-2415. doi: 10.1038/nprot.2006.356.

10. Perrin L, Carmona A, Roudeau S, Ortega R. Evaluation of sample preparation methods for single cell quantitative element imaging using proton or synchrotron radiation focused beams. Journal of Analytical Atomic Spectrometry. 2015, 30, 2525-2532. doi: 10.1039/C5JA00303B

11. Lukinavičius G, Reymond L, D'Este E, Masharina A, Göttfert F, Ta H, Güther A, Fournier M, Rizzo S, Waldmann H, Blaukopf C, Sommer C, Gerlich DW, Arndt HD, Hell SW, Johnsson K. Fluorogenic probes for live-cell imaging of the cytoskeleton. Nat Methods. 2014, 11 (7), 731-733. doi: 10.1038/nmeth.2972.

12. Lukinavičius G, Reymond L, Umezawa K, Sallin O, D'Este E, Göttfert F, Ta H, Hell SW, Urano Y, Johnsson K. Fluorogenic Probes for Multicolor Imaging in Living Cells. Journal of the American Chemical Society. 2016, 138, 9365–9368. doi: 10.1021/jacs.6b04782

13. Chen S, Deng J, Yuan Y, Flachenecker C, Mak R, Hornberger B, Jin Q, Shu D, Lai B, Maser J, Roehrig C, Paunesku T, Gleber SC, Vine DJ, Finney L, VonOsinski J, Bolbat M, Spink I, Chen Z, Steele J, Trapp D, Irwin J, Feser M, Snyder E, Brister K, Jacobsen C, Woloschak G, Vogt S. The

Bionanoprobe: hard X-ray fluorescence nanoprobe with cryogenic capabilities. J. Synchrotron Rad. 2014, 21 (Pt 1), 66-75. doi: 10.1107/S1600577513029676.

14. Vogt S. MAPS: a set of software tools for analysis and visualization of 3D X-ray fluorescence data sets. Journal de Physique IV. 2003, 104, issue 2, 635–638. doi: 10.1051/jp4:20030160.

15. Dunn KW, Kamocka MM, McDonald JH. A practical guide to evaluating colocalization in biological microscopy. Am J Physiol Cell Physiol. 2011 300 (4):C723-42. doi: 10.1152/ajpcell.00462.2010.

16. Schneider C. Rasband W, Eliceiri K. NIH Image to ImageJ: 25 years of image analysis. Nat Methods. 2012, 9, 671–675. doi: 10.1038/nmeth.2089

17. Stauffer W, Sheng H, Lim HN. EzColocalization: An ImageJ plugin for visualizing and measuring colocalization in cells and organisms. Scientific Reports. 2018, 8, 15764. doi: 10.1038/s41598-018-33592-33598

18. Bridgman PC, Dailey ME. The organization of myosin and actin in rapid frozen nerve growth cones. J Cell Biol. 1989, 108 (1), 95-109. doi: 10.1083/jcb.108.1.95.

19. Omotade OF, Pollitt SL, Zheng JQ. Actin-based growth cone motility and guidance. Mol Cell Neurosci. 2017, 84, 4-10. doi: 10.1016/j.mcn.2017.03.001.

20. Sutherland DJ, Pujic Z, Goodhill GJ. Calcium signaling in axon guidance. Trends Neurosci. 2014, 37 (8), 424-432. doi: 10.1016/j.tins.2014.05.008.

21. Kater SB, Mills LR. Regulation of growth cone behavior by calcium. J Neurosci. 1991, 11 (4), 891-899. doi: 10.1523/JNEUROSCI.11-04-00891.1991.

22. Wen Z, Guirland C, Ming GL, Zheng JQ. A CaMKII/calcineurin switch controls the direction of Ca(2+)-dependent growth cone guidance. Neuron. 2004, 43 (6), 835-46. doi: 10.1016/j.neuron.2004.08.037.

23. Pollock NS, Atkinson-Leadbeater K, Johnston J, Larouche M, Wildering WC, McFarlane S. Voltage-gated potassium channels regulate the response of retinal growth cones to axon extension and guidance cues. Eur J Neurosci. 2005, 22 (3), 569-578. doi: 10.1111/j.1460-9568.2005.04242.x.

24. Hutchins BI, Li L, Kalil K. Wnt-induced calcium signaling mediates axon growth and guidance in the developing corpus callosum. Sci Signal. 2012, 5 (206), pt1. doi: 10.1126/scisignal.2002523.

25. Li L, Fothergill T, Hutchins BI, Dent EW, Kalil K. Wnt5a evokes cortical axon outgrowth and repulsive guidance by tau mediated reorganization of dynamic microtubules. Dev Neurobiol. 2014, 74 (8), 797-817. doi: 10.1002/dneu.22102.

26. Tojima T, Akiyama H, Itofusa R, Li Y, Katayama H, Miyawaki A, Kamiguchi H. Attractive axon guidance involves asymmetric membrane transport and exocytosis in the growth cone. Nat Neurosci. 2007, 10 (1), 58-66. doi: 10.1038/nn1814

27. Yao J, Sasaki Y, Wen Z, Bassell GJ, Zheng JQ. An essential role for beta-actin mRNA localization and translation in Ca2+-dependent growth cone guidance. Nat Neurosci. 2006, 9 (10), 1265-73. doi: 10.1038/nn1773.

28. Ortega R, Cloetens P, Devès G, Carmona A, Bohic S. Iron storage within dopamine neurovesicles revealed by chemical nano-imaging. PLoS One. 2007, 2 (9), e925. doi: 10.1371/journal.pone.0000925.

29. Lane DJ, Merlot AM, Huang ML, Bae DH, Jansson PJ, Sahni S, Kalinowski DS, Richardson DR. Cellular iron uptake, trafficking and metabolism: Key molecules and mechanisms and their roles in disease. Biochim Biophys Acta. 2015 May;1853(5):1130-44. doi: 10.1016/j.bbamcr.2015.01.021.

30. De Samber B, Vanden Berghe T, Meul E, Bauters S, Seyrich M, Smet J, De Paepe B, da Silva JC, Bohic S, Cloetens P, Van Coster R, Vandenabeele P, Vincze L. Nanoscopic X-ray imaging and quantification of the iron cellular architecture within single fibroblasts of Friedreich's ataxia patients. J Synchrotron Radiat. 2020 Jan 1;27(Pt 1):185-198. doi: 10.1107/S1600577519015510.

31. Zinsmaier KE, Babic M, Russo GJ. Mitochondrial transport dynamics in axons and dendrites. Results Probl Cell Differ. 2009;48:107-39. doi: 10.1007/400_2009_20.

32. Zivraj KH, Tung YC, Piper M, Gumy L, Fawcett JW, Yeo GS, Holt CE. Subcellular profiling reveals distinct and developmentally regulated repertoire of growth cone mRNAs. J Neurosci. 2010, 30 (46), 15464-78. doi: 10.1523/JNEUROSCI.1800-10.2010.

33. Bastian TW, von Hohenberg WC, Georgieff MK, Lanier LM. Chronic Energy Depletion due to Iron Deficiency Impairs Dendritic Mitochondrial Motility during Hippocampal Neuron Development. J Neurosci. 2019, 39 (5), 802-813. doi: 10.1523/JNEUROSCI.1504-18.2018.

34. Fretham SJ, Carlson ES, Georgieff MK. The role of iron in learning and memory. Adv Nutr. 2011, 2 (2), 112-121. doi: 10.3945/an.110.000190.

35. Adamo AM, Oteiza PI. Zinc deficiency and neurodevelopment: the case of neurons. Biofactors. 2010, 36 (2), 117-124. doi: 10.1002/biof.91.

36. Maxfield L, Shukla S, Crane JS. Zinc Deficiency. [Updated 2021 Aug 13]. In: StatPearls [Internet]. Treasure Island (FL): StatPearls Publishing; 2021 Jan-. Available from: https://www.ncbi.nlm.nih.gov/books/NBK493231/

37. Fimognari N, Hollings A, Lam V, Tidy RJ, Kewish CM, Albrecht MA, Takechi R, Mamo JCL, Hackett MJ. Biospectroscopic Imaging Provides Evidence of Hippocampal Zn Deficiency and Decreased Lipid Unsaturation in an Accelerated Aging Mouse Model. ACS Chem Neurosci. 2018, 9(11), 2774-2785. doi: 10.1021/acschemneuro.8b00193.